High-*κ* monocrystalline dielectrics for low-power two-dimensional electronics

Lei Yin [1,4], Ruiqing Cheng [1,4], Xuhao Wan [2,4], Jiahui Ding [1], Jun Jia [2], Yao Wen[1], Xiaoze Liu [1], Yuzheng Guo [2] ✉ & Jun He [1,3] ✉

The downscaling of complementary metal-oxide-semiconductor technology has produced breakthroughs in electronics, but more extreme scaling has hit a wall of device performance degradation. One key challenge is the development of insulators with high dielectric constant, wide bandgap and high tunnel masses. Here, we show that two-dimensional monocrystalline gadolinium pentoxide, which is devised through combining particle swarm optimization algorithm and theoretical calculations and synthesized via van der Waals epitaxy, could exhibit a high dielectric constant of ~25.5 and a wide bandgap simultaneously. A desirable equivalent oxide thickness down to 1 nm with an ultralow leakage current of ~10^{-4} A cm^{-2} even at 5 MV cm^{-1} is achieved. The molybdenum disulfide transistors gated by gadolinium pentoxide exhibit high on/off ratios over 10^8 and near-Boltzmann-limit subthreshold swing at an operation voltage of 0.5 V. We also constructed inverter circuits with high gain and nanowatt power consumption. This reliable approach to integrating ultrathin monocrystalline insulators paves the way to future nanoelectronics.

The continued shrinking of the physical feature size of metal-oxide-semiconductor field-effect transistors has been the main impetus in the evolution of integrated circuits[1,2]. Such advances are accomplished through several technology developments, including reducing the thickness of channel and gate oxide[3–5]. In particular, the ideal dielectric with a combination of high dielectric constant ($\varepsilon \geq 12$) and wide bandgap ($E_g \geq 5$ eV) is highly desired[6,7]. On the one hand, the use of high-*κ* dielectrics to replace silicon dioxide could greatly reduce the gate leakage and enhance the overall gate controllability on the channel with scaled supply voltage. On the other hand, a wide bandgap allows high dielectric strength and sufficient band offsets (≥1 eV) to minimize conduction by the Schottky emission of carriers into the dielectric bands. However, in typical inorganic dielectrics, the bandgap is inversely proportional to the dielectric constant (Fig. 1a), which is the sum of electronic and ionic contributions[8,9], $\varepsilon = \varepsilon_\infty + \varepsilon_{ion}$. The former, which comes from the reorganization of electronic density, is usually inversely proportional to the bandgap. Thus, any desire to increase the overall dielectric constant in wide-bandgap materials must target the

ionic contribution, which depends principally on the crystal structure and the associated vibrational modes, and does not have to follow the above inverse relation.

In general, metal oxides containing large and highly charged ions have a strong ionic dielectric response. Representatively, HfO$_2$ insulators are the most common high-*κ* dielectrics that work well in current silicon technology, because of the co-existence of large E_g and high ε_{ion}. However, they are amorphous, and far from achieving the theoretically predicted potential owing to their high-density defects and the resulting gate threshold instabilities and electrical breakdown failure[10–13]. In addition, their compatibility with two-dimensional (2D) layered semiconductors still faces many challenges, including inhibited precursor nucleation and rough interfaces[14]. Although some efforts such as introducing seed layers or surface modification have been developed[14–16], the large variability and technique complexity limit its uses. Rare earth oxides have been considered as potential alternatives to conventional dielectrics for transistor applications owing to their superior thermodynamic properties and high conduction

[1]Key Laboratory of Artificial Micro- and Nano-structures of Ministry of Education and School of Physics and Technology, Wuhan University, Wuhan, China. [2]School of Electrical Engineering and Automation, Wuhan University, Wuhan, China. [3]Wuhan Institute of Quantum Technology, Wuhan, China. [4]These authors contributed equally: Lei Yin, Ruiqing Cheng, Xuhao Wan. ✉e-mail: yguo@whu.edu.cn; He-jun@whu.edu.cn
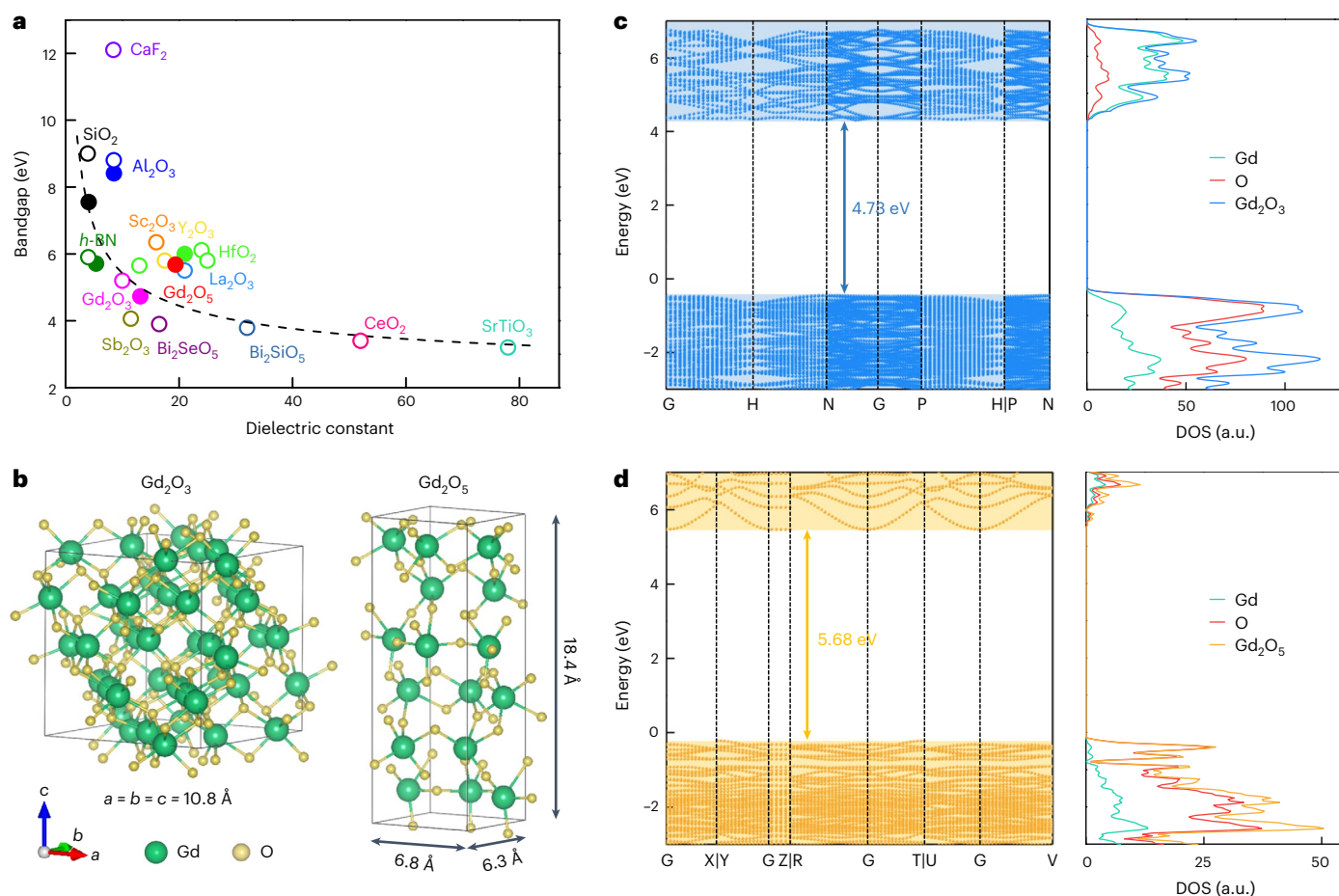
Fig. 1 | Theory calculations. a, Energy bandgap versus dielectric constant of typical insulators[7–15]. The data are from our calculated results (filled symbols) and literature (open symbols, as listed in Supplementary Table 1). The dashed black line is used to guide the eyes, indicating the inversely proportional relationship between the bandgap and the dielectric constant. **b**, The final optimized crystal structures of Gd_2O_3 and Gd_2O_5. **c,d**, Calculated band structures and DOS of Gd_2O_3 and Gd_2O_5 crystals. Gd_2O_5 possesses a wider bandgap than Gd_2O_3. Additionally, the band conduction contribution of Gd_2O_3 mainly comes from Gd atoms (**c**), whereas in Gd_2O_5, the contributions from both elements are more balanced (**d**).

band offset[17,18]. They could even produce an almost fully ionic bonding situation due to the contracted, core-like nature of $4f$ valence orbitals, thus causing large coordination numbers[19]. As shown in Fig. 1a, the dielectric performance of rare earth oxides can be comparable to or even better than the conventional oxides. However, their freestanding single-crystalline membranes have rarely been reported. In addition, the anisotropies of the dielectric constant are also an essential factor for single-crystalline insulators. In Bi_2SeO_5 crystal, for example, the dielectric constant adopted in practice (that is, along the direction normal to the 2D plane) is 16.5, far below the average value along all directions[8].

In this work, we show that ultrathin gadolinium pentoxide (Gd_2O_5) single crystals exhibit a high dielectric constant of ~25.5 and a wide bandgap simultaneously, which is devised through combining the particle swarm optimization (PSO) algorithm and theoretical calculations and synthesized via van der Waals (vdW) epitaxy. Benefitting from the layered supercell structure and high κ value, 2D Gd_2O_5 allows an equivalent oxide thickness (EOT) down to 1 nm with an ultralow leakage of ~10^{-4} A cm^{-2} even at 5 MV cm^{-1}, which is almost the best performance attained in various high-κ dielectrics. Besides, monocrystalline Gd_2O_5 can be integrated with layered semiconductors through vdW force, thus creating a high-quality dielectric–channel interface to enable high-performance 2D transistors. The fabricated MoS_2 transistors exhibit high on/off ratios over 10^8 and near-Boltzmann-limit subthreshold swing (SS) at low operation voltages ($V_{DS} = 0.5$ V and $V_{GS} = 0.4$ V),

as well as superior short-channel effect (SCE) immunity. We also show that the devices can be used to construct inverter circuits with a high gain approaching 40 and a low power consumption of a few nanowatts.

Physical model and theory calculations

Gadolinium oxide films have been widely investigated due to their potential applications as high refractive index materials and high-κ dielectrics. Although Gd is a rare earth metal, its abundance is close to or greater than the values of the elements commonly used in chip manufacturing such as Hf and W (ref. 20). Based on the matching relationship between atomic coordinates and system energy, we performed the PSO algorithm to search for the most stable crystal structures of gadolinium oxides with various stoichiometries (Supplementary Fig. 1). Compared with the recent artificial intelligence material structure discovery algorithms[21], the PSO algorithm does not need to train models based on large datasets, which is more straightforward and less time costly. Based on the structures revealed by intelligence searching, ab initio molecular dynamics simulations were carried out to melt the proposed structures at 2,000 K and then anneal them from 2,000 K down to 300 K to further explore the possible stable structures. Finally, two crystal structures with similar formation energies of −0.6 eV, that is, Gd_2O_3 and Gd_2O_5, were optimized and determined by first-principles calculations (Fig. 1b).

We also calculated the band structures and density of states (DOS) of these two structures using density functional theory (Fig. 1c,d). As shown, Gd_2O_5 possesses a wider bandgap than Gd_2O_3. In terms of

the distribution of energy bands below the Fermi level, they exhibit a fundamental similarity: the upper part of the valence band is predominantly filled, with contributions primarily originating from oxygen element. However, the contrast becomes conspicuous when considering the energy bands above the Fermi level. Due to its lower oxygen content, Gd_2O_3 primarily exhibits conduction band contributions from gadolinium atoms, whereas in Gd_2O_5, the contributions from both elements are more balanced. The dissimilarity in the band structure especially above the Fermi level might be attributed to variations in the coordination number of gadolinium ions and differing oxidation states. As discussed above, the electronic contribution is related to the polarizability of electron density, while the ionic contribution is linked to the degree of ionic polarization[9]. For insulators with a wide bandgap, such as HfO_2, the acquisition of high dielectric constant lies in a strong ion polarization that depends on the ionic properties, such as the size and charge of ions, as well as the degree of ionic bonding. Density functional perturbation theory shows that the electronic contribution of the dielectric constant is similar for these two crystals (Supplementary Fig. 2). However, the ionic contribution of Gd_2O_5 is much higher than the electric contribution. Therefore, Gd_2O_5 crystal could reasonably exhibit a wide bandgap and a high dielectric constant simultaneously.

Synthesis and characterizations

The synthesis of Gd_2O_5 nanosheets was carried out in a home-built chemical vapour deposition (CVD) system, with mica as growth substrate and $GdCl_3$ as gadolinium source (Fig. 2a and Supplementary Fig. 3). Due to the hygroscopicity of $GdCl_3$ powder, atmospheric moisture has a significant impact on the sample synthesis. The domain size of Gd_2O_5 nanosheets increases obviously with the increasing ambient relative humidity. It is worth noting that the introduction of Fe_2O_3, which can drive oxygen atom transfer reactions and effectively enhance the oxidation process[22], is essential. Only GdOCl was obtained at the same growth conditions but without Fe_2O_3 in the precursor (Supplementary Fig. 4). The atomically flat surface of mica brings the absence of anchors to secure bonds between substrate and products, thus leading to a low nucleation density and small migration barrier of adatoms[23]. In addition, the crystal plane (001) of Gd_2O_5 crystal exhibits the lowest surface energy of 21.42 meV $Å^{-2}$, compared with 39.41 meV $Å^{-2}$ and 32.38 meV $Å^{-2}$ of (100) and (010) planes, respectively. Based on the anisotropic surface energies of Gd_2O_5 and the vdW-type migration of adatoms, its 2D anisotropic growth could be activated, and the maximum domain size is over 100 μm (Fig. 2b). It also features atomically smooth surface with root-mean-square roughness less than 0.3 nm, comparable to that of vdW crystals (Supplementary Fig. 5). The crystal size and thickness can be commendably controlled by modulating the growth parameters (Supplementary Fig. 6). Besides, the as-synthesized samples are prone to wrinkling under a small gas flow, suggesting a weak adhesion force between Gd_2O_5 and substrate originated from the vdW epitaxy mechanism (Supplementary Fig. 7). Therefore, through a low-temperature etching-free approach, Gd_2O_5 can be easily separated from the substrate and transferred onto other arbitrary materials.

Electron energy-loss spectroscopy (EELS) was performed to investigate the chemical composition and bandgap of Gd_2O_5 nanosheets (Fig. 2c)[24,25]. Although Fe_2O_3 is introduced during the growth, the nanosheets are composed of Gd and O, and the atomic ratio of Fe element is 0.000%. Furthermore, we analysed the low-loss region in the EELS spectrum and found that the bandgap of a 24-nm-thick sample is ~6.94 ± 0.02 eV (Fig. 2c, inset), which is higher than that of the most crystalline high-κ dielectrics such as $SrTiO_3$ (3.2 eV)[7], Bi_2SeO_5 (3.9 eV)[8], Sb_2O_3 (4.06 eV)[26] and Bi_2SiO_5 (3.79 eV)[27]. Theory calculation shows that the bandgap of Gd_2O_5 increases as the thickness decreases, consistent with the tendency obtained from EELS measurements (Supplementary Fig. 8). In addition, energy-dispersive X-ray spectroscopy (EDS) elemental mappings display the uniform distribution of Gd and O throughout the entire nanosheet (Fig. 2d).

Figure 2e shows an in-plane high-angle annular dark-field scanning transmission electron microscopy (HAADF-STEM) image of Gd_2O_5 nanosheet, exhibiting a highly ordered atomic arrangement. In the light of the image contrast dependence on the atomic number (Z) and the quantity of atoms, the atomic columns containing different quantities of gadolinium ($Z = 64$) are clearly identified. As shown in Fig. 2f and Supplementary Fig. 9, since the quantity of Gd per unit cell in atomic column 1 is twice that in column 2, the former has a more noticeable brightness. Moreover, the brightest spots (atomic column 1) are arranged in pairs, with a dark spot (column 2) on either side of them. In this manner, two different configurations of Gd column are formed and arranged to a rectangular pattern with in-plane lattice parameters of ~6.83 and 6.29 Å, consistent with Gd atomic arrangement in the projected plane along the c axis. The atomic-resolution EDS mapping clearly indicates the in-plane occupation sites of Gd atoms (Fig. 2g). Besides, the selected-area electron diffraction (SAED) pattern along the [001] zone axis shows the corresponding rectangular structure (Fig. 2h).

Further, we prepared two cross-sectional samples that are orthogonal to each other to reveal the out-of-plane atomic structures (Supplementary Fig. 10). As expected, both HAADF-STEM images show a regular layered arrangement (Fig. 2i,j). In the image viewed along the [100] zone axis, the bright dots are also arranged in pairs and form the rectangular pattern like the Gd atomic arrangement viewed along the c-axis direction. Differently, a periodic gap of ~3.3 Å divides the GdO layers into distinguishable ternary layers. Thus, Gd_2O_5 nanosheets are arranged with a period of two ternary GdO layers, corresponding to the out-of-plane lattice parameter ($c = 18.03$ Å) of a unit cell. Notably, these two adjacent ternary layers have the same Gd atomic arrangement along the b-axis direction; thereby, the repetition period of ternary GdO layers is halved to $1/2c$. Moreover, high-resolution transmission electron microscopy images and the corresponding fast Fourier transform patterns are given in Supplementary Fig. 11. The measured interplanar distances of 3.10 Å, 3.44 Å and 9.0 Å correspond to the (020), (200) and (002) planes, respectively. These results confirm the orthorhombic structure of Gd_2O_5. Furthermore, multiple SAED patterns taken from different locations of a sample display nearly identical orientation, suggesting the single-crystalline nature of 2D Gd_2O_5 (Supplementary Fig. 12).

Dielectric and ferroelectric properties

The parallel-plate capacitors with vertical metal–insulator–metal (MIM) structure were fabricated to study the dielectric and ferroelectric properties of Gd_2O_5. The corresponding capacitance–voltage (C–V) measurements at various frequencies (f) are shown in Supplementary Fig. 13. The effective dielectric constant (ε_{eff}) of Gd_2O_5 nanosheets can be calculated by the equation[13] $C = A\varepsilon_{eff}\varepsilon_0/t_{ox}$, where C is the measured capacitance, A is the overlapping area of top and bottom electrodes, ε_0 is the vacuum dielectric constant and t_{ox} is the physical thickness of Gd_2O_5. As shown in Fig. 3a, the ε_{eff} of ~32 nm Gd_2O_5 is around 25.5 at 50 kHz and gradually decreases with the applied frequency. Notably, although the frequency range of the ionic contribution is slower than that of the electronic contributions according to the conventional dielectric spectroscopy graph, the decreasing trend almost stops at 0.5 MHz (Supplementary Fig. 13), implying the potential of Gd_2O_5 for high-frequency applications. Compared with most crystalline dielectrics (such as h-BN, Bi_2SeO_5 and Sb_2O_3), Gd_2O_5 has both a higher ε_{eff} and a wider bandgap. Furthermore, the statistical ε_{eff} of Gd_2O_5 with different thicknesses at $f = 50$ kHz is plotted in Fig. 3b, which shows a decreasing trend with the thickness reduction and can be well fitted by the typical 'dead layer' model owing to the presence of interfacial capacitance[13,27]. The corresponding EOT, calculated by $3.9 t_{ox}/\varepsilon_{eff}$, shows a linear relationship with the thickness, suggesting that a 1 nm EOT can be realized when the thickness is reduced to ~5 nm.

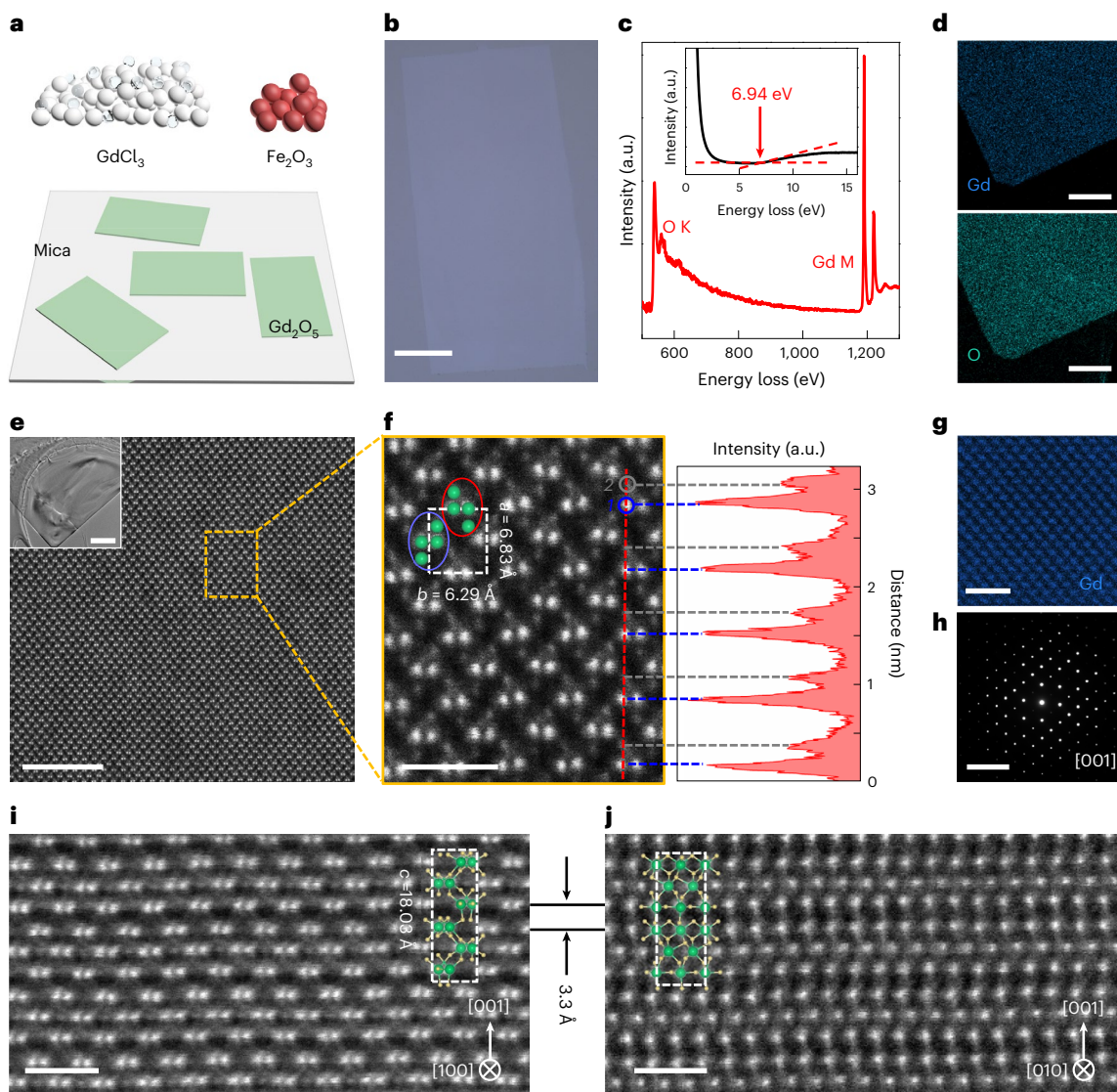**Fig. 2 | Growth and characterizations of 2D Gd$_2$O$_5$. a**, vdW epitaxial growth of Gd$_2$O$_5$ nanosheets. **b**, An OM image of an as-grown Gd$_2$O$_5$ nanosheet with a domain size over 100 μm. Scale bar, 20 μm. **c**, EELS spectrum of O K core-level edge and Gd M core-level edge. The inset is the plot of low-loss EELS spectrum, defining a bandgap of 6.94 eV. **d**, STEM–EDS elemental mapping images of Gd$_2$O$_5$ nanosheet. Scale bars, 0.5 μm. **e**, An in-plane atomic-resolution HAADF-STEM image of an ultrathin Gd$_2$O$_5$ (scale bar, 5 nm). The inset is the corresponding low-magnification morphology image (scale bar, 1 μm). **f**, A high-magnification HAADF-STEM image of the nanosheet and the intensity profile along the dashed red line. The blue and grey circles denote two different Gd atomic columns ('1' and '2') with a noticeable brightness contrast. The green balls indicate the

Gd atomic arrangement in the projected plane along the *c* axis, where two different configurations of Gd are formed and circled by red and purple ellipses. The dashed white rectangle indicates a unit cell of Gd$_2$O$_5$. Scale bar, 1 nm. **g**, An atomic-resolution EDS mapping of Gd$_2$O$_5$ nanosheet. Scale bar, 2 nm. **h**, SAED pattern of Gd$_2$O$_5$ nanosheet, demonstrating its rectangular structure. Scale bar, 5 nm⁻¹. **i**,**j**, Cross-sectional HAADF-STEM images of Gd$_2$O$_5$ nanosheet, which is consistent with the atomic arrangement in the projected plane along the *a* axis (**i**) and the *b* axis (**j**). The distance between two adjacent GdO ternary layers is ~3.3 Å. Scale bars, 1 nm. The insets are the side view of the Gd$_2$O$_5$ structure model. The green and yellow balls represent Gd and O atoms, respectively.

The leakage current and breakdown field strength (E_{BD}) in vertical MIM devices with various Gd$_2$O$_5$ thicknesses is given in Fig. 3c and Supplementary Fig. 14. All devices have an E_{BD} in the range of 6.9–15.7 MV cm⁻¹, verifying the reliability of 2D Gd$_2$O$_5$ as dielectrics. For 5.2-nm-thick Gd$_2$O$_5$ (EOT ~1 nm), the leakage current density of ~10⁻⁴ A cm⁻² is less than the low-power limit (1.5×10^{-2} A cm⁻²) even at the applied electric field of 5 MV cm⁻¹ (Supplementary Fig. 14). By contrast, the leakage of 8.4 nm SrTiO$_3$ dielectric is ~10⁻¹ A cm⁻² at 2 MV cm⁻¹ (ref. 13). It should be noted that E_{BD} is also closely related to the crystal quality and testing methods, causing a variation in the E_{BD} of the same material. The E_{BD} values acquired by standard device measurement (SDM) are more objective for evaluating the practical application potential of dielectric materials. Thus, we summarized

the E_{BD} obtained by SDM and the corresponding dielectric constant of common dielectrics[26–34]. As shown in Fig. 3d, there is an inverse relationship between E_{BD} and the dielectric constant, as described by $E_{BD} \sim \varepsilon^{-0.5}$ (ref. 28). In particular, although amorphous HfO$_2$ has a large bandgap, its E_{BD} values are less than 10 MV cm⁻¹ owing to the potential leakage pathways associated with defects. In contrast, Gd$_2$O$_5$ single crystals with relatively large bandgap and increased ionicity allow the co-existence of high dielectric constant and high E_{BD}. In addition, the dielectric constant of Gd$_2$O$_5$ is almost isotropic, which could effectively screen the Coulomb potentials of charged impurities and ensure its practical applications (Supplementary Table 2)[8].

The non-zero second-harmonic generation signal of 2D Gd$_2$O$_5$ suggests the broken inversion symmetry, which is a prerequisite for
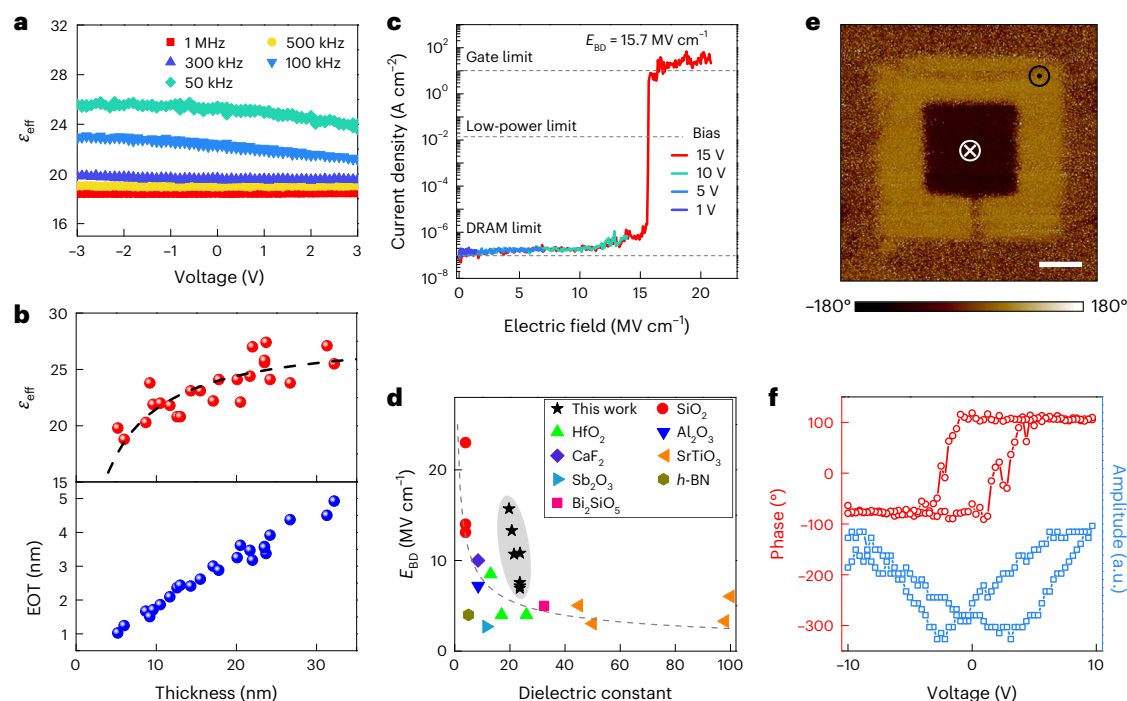
Fig. 3 | Dielectric and ferroelectric properties of 2D Gd$_2$O$_5$. a, The ε_{eff} of ~32 nm Gd$_2$O$_5$ at various frequencies measured using MIM structure. $A \approx 126.5$ μm^2. **b**, The statistical ε_{eff} of Gd$_2$O$_5$ nanosheets with different thicknesses at $f = 50$ kHz and the corresponding EOT. The dashed black line is the fitted curve using the 'dead layer' model. **c**, Leakage current density as a function of electric field for a vertical graphite/7.2-nm-thick Gd$_2$O$_5$/metal device. $A \approx 5.6$ μm^2. The dashed lines mark the limits for various electronic applications. DRAM, dynamic random access memory. **d**, E_{BD} versus dielectric constant of various common dielectrics[26–34]. The E_{BD} values are from the SDMs, and the dielectric constant values are estimated by the fitted curves in **b**. The dashed grey line indicates the inversely proportional relationship between the dielectric constant and E_{BD}. **e**, The PFM phase of a 24-nm-thick Gd$_2$O$_5$ nanosheet with a written box-in-box pattern using voltage biases of ±10 V. Scale bar, 2 μm. **f**, PFM phase and amplitude hysteresis loops of 2D Gd$_2$O$_5$.

inducing ferroelectric polarization (Supplementary Fig. 15). To identify the ferroelectricity, we measured the polarization–electric field (P–E) loops of Gd$_2$O$_5$ parallel-plate capacitors at room temperature, which exhibits ferroelectric switching behaviour like hafnium-based ferroelectrics[35,36]. As shown in Supplementary Fig. 16, the P–E curves indicate hysteresis loops and obvious remnant polarization at zero field, verifying the room-temperature ferroelectricity of Gd$_2$O$_5$. The remnant polarization value of 5.8 μC cm^{-2} obtained at 10 kHz is comparable to that of some typical ferroelectrics[37–39]. Besides, thickness reduction in Gd$_2$O$_5$ would cause the depolarization field, giving rise to a reduction in remnant polarization[37]. The ferroelectric feature is further confirmed by C–V hysteresis (Supplementary Fig. 17) and piezoresponse force microscopy (PFM; Fig. 3e,f and Supplementary Figs. 18–20). Figure 3e shows the out-of-plane PFM phase of ferroelectric domains written on Gd$_2$O$_5$, indicating a clear phase contrast and good retention. The PFM phase and amplitude hysteresis loops show a 180° phase flip and a well-defined butterfly shape (Fig. 3f). These results manifest the switchable ferroelectric polarization of Gd$_2$O$_5$ nanosheets.

Monocrystalline dielectric for 2D transistors

To examine the gate dielectric performance, monocrystalline Gd$_2$O$_5$ was integrated with 2D semiconductors to enable top-gated transistors using vdW forces (Fig. 4a and Supplementary Fig. 21). On the one hand, the formed vdW gap through physical stacking increases the distance between channel and dielectric, thus weakening the interaction between them and enabling semiconductor channel to preserve the intrinsic properties[10]. On the other hand, the mild integration process creates a high-quality channel–dielectric interface in transistors, which could reduce the carrier scattering and suppress the gate leakage[13]. Figure 4b shows the cross-sectional STEM image and EDS mapping of transistor channel area, indicating a vdW gap of ~4.1 Å as well as a

clean interface without any structural disorder. Figure 4c shows the transfer curves of a few-layer (FL) MoS$_2$ field-effect transistor (FET) with 8.5-nm-thick Gd$_2$O$_5$ dielectric and graphite top electrode. The optical microscopy (OM) and atomic force microscopy (AFM) images are given in Supplementary Fig. 22. The transistor exhibits a high on/off ratio of ~10^8 and low SS of 61.5 mV dec^{-1} within an ultranarrow V_{GS} range from 0.4 to −0.6 V. Moreover, the gate leakage is as low as 10^{-7} A cm^{-2}, which fulfils the low-power specification and is far below that gated by 16.4 nm SrTiO$_3$ (ref. 13). The corresponding output curves are linear at a small V_{DS}, while gradually saturating as V_{DS} increases owing to the pinch-off of the MoS$_2$ channel (Fig. 4d).

Note that the dual-sweep transfer characteristics exhibit anticlockwise hysteresis due to the dipole polarization in ferroelectric Gd$_2$O$_5$ (Supplementary Fig. 23). The small hysteresis is consistent with the low remanent polarization in thin Gd$_2$O$_5$ dielectric. Through double-gate measurements, we derived its top-gated capacitance and extracted the dielectric constant of 19.7 (Supplementary Fig. 24), which is almost consistent with that obtained by capacitance measurement on MIM devices (Fig. 3b). The trap density (D_{it}) is extracted according to the following equation[13]: $SS = \ln(10) \frac{k_B T}{q} \left(1 + \frac{q D_{it}}{C_{ox}}\right)$, where T is temperature, k_B is the Boltzmann constant, q is elementary charge and C_{ox} is the capacitance of the gate dielectric. The extracted D_{it} is about 2.2×10^{12} cm^{-2} eV^{-1} and comparable to the values in MoS$_2$ devices with conventional oxides[17]. Benefitting from the encapsulation of channel within Gd$_2$O$_5$, the MoS$_2$ transistor exhibits excellent stability (Supplementary Fig. 25).

Moving towards a smaller EOT, we fabricated top-gated monolayer (ML) MoS$_2$ FETs adopting ~6.5 nm Gd$_2$O$_5$ as the gate dielectrics (Supplementary Figs. 26 and 27). Efficient switching with a steep SS down to 64 mV dec^{-1}, a high on/off ratio of ~10^6 and a negligible
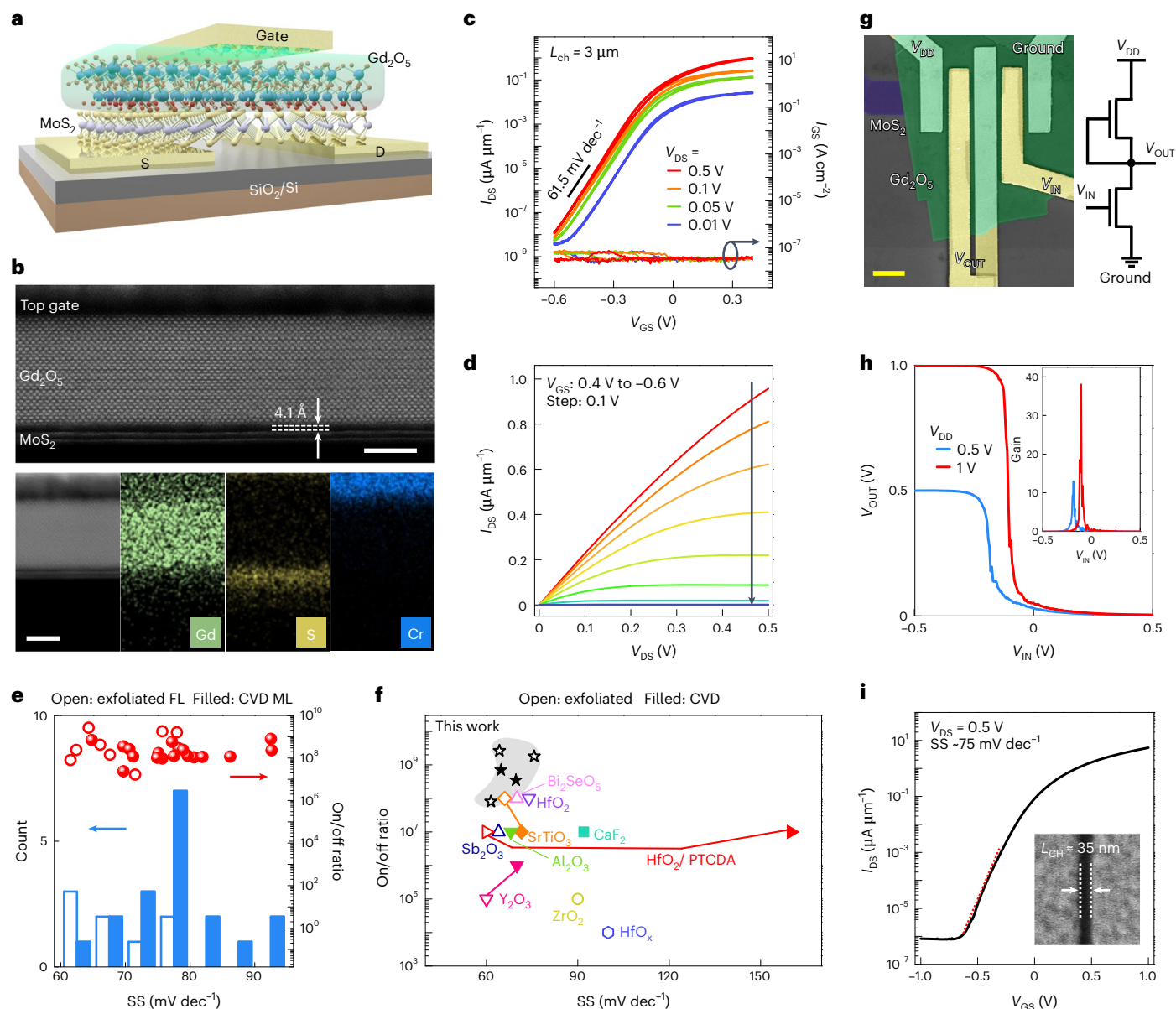
Fig. 4 | Gd$_2$O$_5$ dielectrics for high-performance 2D transistors. a, A schematic of the top-gated MoS$_2$ FETs. S, source; D, drain. **b**, A cross-sectional STEM image (top) and EDS elemental mapping images (bottom) of the transistor channel area, where a clean interface with a vdW gap of ~4.1 Å exists between the MoS$_2$ channel and Gd$_2$O$_5$ dielectric. Scale bars, 5 nm. **c**, Dual-sweep I_{DS}–V_{GS} curves of a MoS$_2$ FET using the graphite top electrode under various V_{DS}. **d**, The corresponding I_{DS}–V_{DS} curves. **e**, A statistical histogram of SS (left axis) measured from exfoliated FL MoS$_2$ FETs (open symbol) and CVD-grown ML MoS$_2$ FETs (filled symbol), as well as

their on/off ratios (right axis). **f**, A performance comparison among the state-of-the-art MoS$_2$ transistors with high-κ dielectrics in terms of SS and on/off ratios[8,13,15,26,40–46]. **g**, A false-coloured SEM image and equivalent circuit of the logic NOT gate (inverter) consisting of two top-gated MoS$_2$ FETs. Scale bar, 3 μm. **h**, Output voltage and gain (inset) as a function of input voltage of the inverter under V_{DD} = 0.5 and 1 V. **i**, I_{DS}–V_{GS} curve of the short-channel MoS$_2$ FET. The inset is an SEM image of the pre-prepared short channel (~35 nm) before the fabrication of the top-gate electrode.

leakage of 10^{-14} A is still achieved at an ultranarrow V_{GS} range. Through double-gate measurements, the extracted EOT of the top-gate dielectric layer is 0.94 nm. Further, a top-gated FET array was fabricated utilizing the CVD-grown ML MoS$_2$, which exhibits good performance uniformity (Supplementary Fig. 28). Figure 4e summarizes the SS and on/off ratios of multiple top-gated MoS$_2$ transistors, and most exhibit high on/off ratios over 10^8 and near-Boltzmann-limit SS. The histograms for threshold voltage and turn-on current density are shown in Supplementary Fig. 29. By comparison with the state-of-the-art MoS$_2$ transistors with high-κ dielectrics[8,13,15,26,40–46], our devices have stronger gate controllability, whether for exfoliated or CVD-grown MoS$_2$ (Fig. 4f and Supplementary Table 3). The mobility of FETs is discussed in Supplementary Fig. 30. Next, we constructed a logic NOT

gate (inverter) consisting of two top-gated MoS$_2$ FETs in series for evaluating the potential of our transistors in digital circuits (Fig. 4g). Benefitting from the superior electrostatic modulation, a high gain approaching 40 and a low power consumption of a few nanowatts are obtained (Fig. 4h and Supplementary Fig. 31), which are comparable to the most reported MoS$_2$ inverters (Supplementary Table 4) and enough to trigger the cascade of multiple logic circuits. The performance could be further improved by optimizing the quality of the MoS$_2$ and electrical contact interface to obtain good output saturation and high transconductance. In addition, SCEs are intensified with the ongoing shrinking of transistor feature sizes[15]. To this end, we fabricated short-channel MoS$_2$ FETs with Gd$_2$O$_5$ as dielectrics. Figure 4i and Supplementary Fig. 32 show the transfer and output characteristics of

the device ($L_{ch} \approx 35$ nm, $t_{ox} = 8.7$ nm). The realized high on/off ratio of 10^7 and steep SS of 75 mV dec^{-1} imply an effective shielding for SCEs.

Conclusions

We have reported the synthesis of ultrathin layered Gd_2O_5 single crystals possessing high κ value and wide bandgap, which is in a highly desirable position compared with the state-of-the-art dielectrics. On the one hand, 2D Gd_2O_5 exhibits an ultralow leakage and a high breakdown voltage, allowing its EOT to be reduced to 1 nm. On the other hand, 2D FET devices fabricated by vdW integration of MoS_2 and Gd_2O_5 exhibit high on/off ratios over 10^8 and near-Boltzmann-limit SS. We also created inverter circuits with high gain and low power consumption. These results suggest that monocrystalline Gd_2O_5 could provide possibilities for 2D nanoelectronics. Industry-compatible applications require scalable synthesis and integration. Our process has been demonstrated to be compatible with the large-area CVD-grown MoS_2 films (Supplementary Fig. 28). Developing the growth techniques of Gd_2O_5 over the whole wafer, however, is less mature and could be a key topic in the foreseeable future. Furthermore, the current mechanical stacking process is challenged by low alignment accuracy and yields, requiring more advanced and efficient industry tools such as precision mechanics and computer-aided control systems for large-scale integration.

Online content

Any methods, additional references, Nature Portfolio reporting summaries, source data, extended data, supplementary information, acknowledgements, peer review information; details of author contributions and competing interests; and statements of data and code availability are available at https://doi.org/10.1038/s41563-024-02043-3.

References

1. Liu, Y. et al. Promises and prospects of two-dimensional transistors. *Nature* **591**, 43–53 (2021).
2. Datta, S., Chakraborty, W. & Radosavljevic, M. Toward attojoule switching energy in logic transistors. *Science* **378**, 733–740 (2022).
3. Choi, Y. K. et al. Ultrathin-body SOI MOSFET for deep-sub-tenth micron era. *IEEE Electron Device Lett.* **21**, 254–255 (2000).
4. Zhang, Y. et al. A single-crystalline native dielectric for two-dimensional semiconductors with an equivalent oxide thickness below 0.5 nm. *Nat. Electron.* **5**, 643–649 (2022).
5. Hisamoto, D. et al. FinFET—a self-aligned double-gate MOSFET scalable to 20 nm. *IEEE Trans. Electron Devices* **47**, 2320–2325 (2000).
6. Robertson, J. High dielectric constant gate oxides for metal oxide Si transistors. *Rep. Prog. Phys.* **69**, 327–396 (2006).
7. Wang, S. et al. Two-dimensional devices and integration towards the silicon lines. *Nat. Mater.* **21**, 1225–1239 (2022).
8. Zhang, C. et al. Single-crystalline van der Waals layered dielectric with high dielectric constant. *Nat. Mater.* **22**, 832–837 (2023).
9. Le Bahers, T., Rérat, M. & Sautet, P. Semiconductors used in photovoltaic and photocatalytic devices: assessing fundamental properties from DFT. *J. Phys. Chem. C* **118**, 5997–6008 (2014).
10. Luo, P. et al. Molybdenum disulfide transistors with enlarged van der Waals gaps at their dielectric interface via oxygen accumulation. *Nat. Electron.* **5**, 849–858 (2022).
11. Robertson, J. & Wallace, R. M. High-K materials and metal gates for CMOS applications. *Mater. Sci. Eng. R. Rep.* **88**, 1–41 (2015).
12. Hong, S. et al. Ultralow-dielectric-constant amorphous boron nitride. *Nature* **582**, 511–514 (2020).
13. Huang, J.-K. et al. High-κ perovskite membranes as insulators for two-dimensional transistors. *Nature* **605**, 262–267 (2022).
14. Zou, X. et al. Interface engineering for high-performance top-gated MoS_2 field-effect transistors. *Adv. Mater.* **26**, 6255–6261 (2014).
15. Li, W. et al. Uniform and ultrathin high-κ gate dielectrics for two-dimensional electronic devices. *Nat. Electron.* **2**, 563–571 (2019).
16. Xu, Y. et al. Scalable integration of hybrid high-κ dielectric materials on two-dimensional semiconductors. *Nat. Mater.* **22**, 1078–1084 (2023).
17. Illarionov, Y. Y. et al. Insulators for 2D nanoelectronics: the gap to bridge. *Nat. Commun.* **11**, 3385 (2020).
18. Wang, B. et al. High-k gate dielectrics for emerging flexible and stretchable electronics. *Chem. Rev.* **118**, 5690–5754 (2018).
19. Cheisson, T. & Schelter, E. J. Rare earth elements: Mendeleev's bane, modern marvels. *Science* **363**, 489–493 (2019).
20. Voncken, J. H. L. *The Rare Earth Elements: An Introduction* (Springer, 2016).
21. Merchant, A. et al. Scaling deep learning for materials discovery. *Nature* **624**, 80–85 (2023).
22. Zhao, Y. et al. α-Fe_2O_3 as a versatile and efficient oxygen atom transfer catalyst in combination with H_2O as the oxygen source. *Nat. Catal.* **4**, 684–691 (2021).
23. Cheng, R. et al. Ultrathin single-crystalline CdTe nanosheets realized via van der Waals epitaxy. *Adv. Mater.* **29**, 1703122 (2017).
24. Yang, K. et al. Ultrathin high-κ antimony oxide single crystals. *Nat. Commun.* **11**, 2502 (2020).
25. Zavabeti, A. et al. A liquid metal reaction environment for the room-temperature synthesis of atomically thin metal oxides. *Science* **358**, 332–335 (2017).
26. Liu, K. et al. A wafer-scale van der Waals dielectric made from an inorganic molecular crystal film. *Nat. Electron.* **4**, 906–913 (2021).
27. Chen, J. et al. Vertically grown ultrathin Bi_2SiO_5 as high-κ single-crystalline gate dielectric. *Nat. Commun.* **14**, 4406 (2023).
28. McPherson, J., Kim, J., Shanware, A., Mogul, H. & Rodriguez, J. Proposed universal relationship between dielectric breakdown and dielectric constant. In *Digest. International Electron Devices Meeting* 633–636 (IEEE, 2002).
29. Kang, L. et al. Electrical characteristics of highly reliable ultrathin hafnium oxide gate dielectric. *IEEE Electron Device Lett.* **21**, 181–183 (2000).
30. Sokolov, N. S. et al. Low-leakage MIS structures with 1.5-6 nm CaF_2 insulating layer on Si(111). *Microelectron. Eng.* **84**, 2247–2250 (2007).
31. Sire, C., Blonkowski, S., Gordon, M. J. & Baron, T. Statistics of electrical breakdown field in HfO_2 and SiO_2 films from millimeter to nanometer length scales. *Appl. Phys. Lett.* **91**, 242905 (2007).
32. Zhang, L. et al. ALD preparation of high-k HfO_2 thin films with enhanced energy density and efficient electrostatic energy storage. *RSC Adv.* **7**, 8388–8393 (2017).
33. Baumert, B. A. et al. Characterization of sputtered barium strontium titanate and strontium titanate-thin films. *J. Appl. Phys.* **82**, 2558–2566 (1997).
34. Kim, S. M. et al. Synthesis of large-area multilayer hexagonal boron nitride for high material performance. *Nat. Commun.* **6**, 8662 (2015).
35. Zhou, C. et al. Enhanced polarization switching characteristics of HfO_2 ultrathin films via acceptor–donor co-doping. *Nat. Commun.* **15**, 2893 (2024).
36. Nukala, P. et al. Reversible oxygen migration and phase transitions in hafnia-based ferroelectric devices. *Science* **372**, 630–635 (2021).
37. Jiang, Y. et al. Enabling ultra-low-voltage switching in $BaTiO_3$. *Nat. Mater.* **21**, 779–785 (2022).
38. Hu, Y. et al. Ferroelastic-switching-driven large shear strain and piezoelectricity in a hybrid ferroelectric. *Nat. Mater.* **20**, 612–617 (2021).
39. Wang, X. et al. Van der Waals engineering of ferroelectric heterostructures for long-retention memory. *Nat. Commun.* **12**, 1109 (2021).
40. Wang, L. et al. A general one-step plug-and-probe approach to top-gated transistors for rapidly probing delicate electronic materials. *Nat. Nanotechnol.* **17**, 1206–1213 (2022).

41. Yang, A. J. et al. Van der Waals integration of high-*κ* perovskite oxides and two-dimensional semiconductors. *Nat. Electron.* **5**, 233–240 (2022).

42. Illarionov, Y. Y. et al. Ultrathin calcium fluoride insulators for two-dimensional field-effect transistors. *Nat. Electron.* **2**, 230–235 (2019).

43. Peimyoo, N. et al. Laser-writable high-*k* dielectric for van der Waals nanoelectronics. *Sci. Adv.* **5**, eaau0906 (2019).

44. Lu, Z. et al. Wafer-scale high-*κ* dielectrics for two-dimensional circuits via van der Waals integration. *Nat. Commun.* **14**, 2340 (2023).

45. Jin, Y. et al. Controllable oxidation of ZrS_2 to prepare high-*κ*, single-crystal m-ZrO_2 for 2D electronics. *Adv. Mater.* **35**, 2212079 (2023).

46. Radisavljevic, B., Radenovic, A., Brivio, J., Giacometti, V. & Kis, A. Single-layer MoS_2 transistors. *Nat. Nanotechnol.* **6**, 147–150 (2011).

Methods

Synthesis of 2D Gd_2O_5 single crystals

The synthesis was carried out in a 1-inch-diameter quartz tube by CVD. The powder of hygroscopic gadolinium trichloride ($GdCl_3$, 99.99%) and ferric oxide (α-Fe_2O_3, 99.5%) was used as the precursors and loaded in a quartz boat, which was then placed in the centre of the furnace heating zone. Freshly cleaved fluorophlogopite mica [$KMg_3(AlSi_3O_{10})F_2$] sheets were placed in the downstream of the tube furnace to serve as epitaxial substrates. High-purity Ar gas (99.999%) with a flow rate of 100 sccm was used as the carrier gas. Then, the furnace was heated from room temperature to 680 °C in 15 min and maintained at this temperature for another 5 min for sample growth. After the reaction completed, the tube furnace naturally cooled down to room temperature.

Sample transfer and characterizations

For transferring, poly(propylene carbonate) (PPC) was first spin-coated onto the mica for carrying the samples. After baking on a hot plate with 90 °C for 2 min, the PPC-capped substrate was placed in deionized water and then the PPC film with samples was lifted off the mica. Subsequently, the film was supported with the needed substrates (such as copper grid and silicon substrate), followed by drying it on a hot plate (90 °C for 10 min). Finally, the PPC covering the samples was removed using hot acetone (70 °C for 10 min). The morphology and thickness of Gd_2O_5 nanosheets were characterized by OM (BX51M, Olympus) and AFM (Dimension Icon, Bruker) under the atmospheric environment, respectively. Transmission electron microscopy images and SAED patterns were obtained on JEM-F200. HAADF-STEM, SAED patterns, EDS mapping and EELS spectra were acquired via a JEOL-ARM200F microscope with a cold-field emission gun. PFM measurements were performed using AFM (Dimension Icon, Bruker) under off-resonance mode, where a stiff tip with a spring constant of ~80 N m^{-1} was driven at 15 kHz.

Device fabrication and characterizations

Both the parallel-plate capacitors and FETs were fabricated on SiO_2/Si substrates. For the parallel-plate capacitors with MIM structure, Gd_2O_5 nanosheets were first transferred onto the pre-prepared bottom electrodes (5/40 nm Cr/Au). Subsequently, the top electrodes (Cr/Au or Au) were defined and deposited via standard electron beam lithography and thermal evaporation apparatus. For top-gated MoS_2 FETs, the drain–source electrode pair (5/30 nm Cr/Au) was first deposited on SiO_2/Si substrates. Then, the exfoliated or CVD-grown MoS_2 and Gd_2O_5 nanosheets were sequentially transferred onto the electrode pair. Finally, exfoliated graphite or 5/60 nm Cr/Au was transferred or deposited onto the Gd_2O_5 as the gate electrode, followed by a lift-off process. Electrical characterizations of FETs and capacitors were performed using a Keithley 4200 semiconductor analyser equipped with capacitance–voltage modules in a vacuum (~10^{-6} Torr) probe station (Lakeshore, TTP4). Polarization–electric field measurement was carried out on a micromanipulated probe station under the atmospheric environment using a Radiant ferroelectric analyser. All the electrical measurements were conducted at room temperature unless otherwise specified.

Structural searches and optimizations

Using the CALYPSO structural prediction software suite[47], a global structural prediction for the Gd_xO_y ($x = $ ~1–2, $y = $ 1–3) system is generated, incorporating ab initio total energy calculations to identify the global energy minima. During this study, lattice parameters and positions of specific atoms derived from the initial structures were fixed. This allowed for further structural derivations and optimizations. To guarantee a thorough and detailed prediction range, a protocol where each generation comprised 50 structures, spanning 50 generations of prediction and screening, is established. In addition to considering the monomer formula units, the investigation also extended to dimer and tetramer formula units, aiming to elucidate a broader spectrum of potential stable configurations for the system. Molecular Orbital PACkage (MOPAC) 2016[48], a semiempirical quantum chemistry simulation program including the PM7 (semiempirical Hamiltonian) method[49], was employed to perform the dynamic annealing process. MOPAC uses a large unit cell called a 'cluster' and adopts the Born–von Kármán periodic boundary conditions. Dynamic reaction coordinate simulation, a molecular dynamics method[50], was conducted for annealing simulation. The annealing process was divided into two sections, first ramping up from 0 K to 2,000 K and then cooling down to 300 K. The warming and cooling process simulation both lasted for 2 ps, with a 1 fs interval and a total of 2,000 steps. The half-life for the loss of kinetic energy was 50 fs.

Density functional theory calculations

The Vienna ab initio simulation package was utilized for conducting first-principles calculations[51]. The interaction between ions and electrons was described using the projector augmented wave basis set[52]. To account for exchange–correlation effects, both the Perdew–Burke–Ernzerhof functional within the generalized gradient approximation and the Heyd–Scuseria–Ernzerhof (HSE06) hybrid functional were applied[53,54]. For ensuring accurate results, a cut-off energy of 520 eV and a self-consistent convergence threshold of 10^{-6} eV were set for energy minimization. During the structural optimization process, the positions of individual atoms were adjusted until the forces on them were less than 0.02 eV Å^{-1}. This criterion ensured thorough relaxation of atomic positions. The Γ centre $3 \times 3 \times 1$ Monkhorst–Pack grid k-point sampling mesh was adopted in optimization, while a denser $5 \times 5 \times 3$ Monkhorst–Pack grid was applied for electronic structure calculations. The empirical Grimme's scheme (DFT-D3) was employed to deal with the vdW interactions[55]. To avoid the influence of interlayer interactions on the surface energy calculations, a vacuum of 15 Å was added in the z direction of each slab model. The expression of surface energy is shown as

$$\gamma = \frac{E_S^0 - NE_B}{2A} + \frac{E_S - E_S^0}{A},$$

where E_S^0 and E_S indicate the total energy of the slab before and after relax, respectively; N indicates the number of atoms in slab model; E_B represents the total energy of the Gd and O atoms; and A represents the surface area of the slab model. The dielectric constants distinguishing the ionic contribution from the electronic contribution in each direction and the corresponding frequency-dependent dielectric functions for semiconductors considering local field effects are calculated using independent particle approximation[56].

Data availability

The data that support the findings of this study are available from the corresponding authors upon reasonable request. Source data are provided with this paper.

References

47. Wang, Y. et al. CALYPSO: a method for crystal structure prediction. *Comput. Phys. Commun.* **183**, 2063–2070 (2012).
48. Stewart, J. J. P. MOPAC: a semiempirical molecular orbital program. *J. Comput. Aided Mol. Des.* **4**, 1–103 (1990).
49. Hostaš, J., Řezáč, J. & Hobza, P. On the performance of the semiempirical quantum mechanical PM6 and PM7 methods for noncovalent interactions. *Chem. Phys. Lett.* **568**, 161–166 (2013).
50. Dieter, K. M. & Stewart, J. J. P. Calculation of vibrational frequencies using molecular trajectories. *J. Mol. Struct. THEOCHEM* **163**, 143–149 (1988).

51. Kresse, G. & Furthmüller, J. Efficient iterative schemes for ab initio total-energy calculations using a plane-wave basis set. *Phys. Rev. B* **54**, 11169 (1996).

52. Blöchl, P. E. Projector augmented-wave method. *Phys. Rev. B* **50**, 17953 (1994).

53. Perdew, J. P., Burke, K. & Ernzerhof, M. Generalized gradient approximation made simple. *Phys. Rev. Lett.* **77**, 3865 (1996).

54. Heyd, J. & Scuseria, G. E. Efficient hybrid density functional calculations in solids: assessment of the Heyd–Scuseria–Ernzerhof screened Coulomb hybrid functional. *J. Chem. Phys.* **121**, 1187–1192 (2004).

55. Grimme, S. Semiempirical GGA-type density functional constructed with a long-range dispersion correction. *J. Comput. Chem.* **27**, 1787–1799 (2006).

56. Sipe, J. E. & Ghahramani, E. Nonlinear optical response of semiconductors in the independent-particle approximation. *Phys. Rev. B* **48**, 11705 (1993).

Acknowledgements

Author contributions

J.H. supervised the project. L.Y. and R.C. conceived and designed the experiments. L.Y. synthesized the sample, performed material characterization, fabricated the devices and performed electrical measurements. X.W., J.J. and Y.G. carried out the theoretical modelling. R.C., J.D., Y.W. and X.L. assisted in the material characterization. L.Y., R.C. and J.H. analysed the data and co-wrote the paper in consultation with all the other authors.

Competing interests

The authors declare no competing interests.

Additional information

Supplementary information The online version contains supplementary material available at https://doi.org/10.1038/s41563-024-02043-3.

Correspondence and requests for materials should be addressed to Yuzheng Guo or Jun He.

Peer review information *Nature Materials* thanks Sang-Hoon Bae, Adrian Ionescu and Soon-Yong Kwon for their contribution to the peer review of this work.

Reprints and permissions information is available at www.nature.com/reprints.